Chemical Science

ROYAL SOCIETY OF CHEMISTRY

EDGE ARTICLE

View Article Online
View Journal | View Issue

Cite this: *Chem. Sci.*, 2025, **16**, 16678

All publication charges for this article have been paid for by the Royal Society of Chemistry

Rational phosphating layer design in biomass-derived hard carbons toward fast charging capability of sodium ion battery anodes

Haihan Zhang,[a] Zhenxin Huang,[a] Siyuan Lin,[a] Jiawu Cui,[a] Qianyu Zhang,*[c] Xiansheng Luo,[d] Rui Wang,[d] Chaofeng Zhang,*[d] Chengyong Shu[a] and Wei Tang*[ab]

Continuous side reactions between a biomass-derived hard carbon (HC) surface and the electrolyte affect its cycling stability and fast-charging performance. Therefore, constructing a stable solid electrolyte interface (SEI) while facilitating easier desolvation of sodium ions in the electrolyte is key to achieving stable fast charging. Theoretical calculations confirmed that Na_3P can induce the formation of a Na^+ solvation structure with low solvent coordination, thus achieving a lower desolvation energy barrier and faster Na^+ diffusion capability through the SEI. We used bamboo powder, partially de-lignified, as a precursor for hard carbon. After sublimating red phosphorus in a sealed tube with deposition upon cooling, a phosphide layer was constructed on the hard carbon surface. During charge–discharge cycling, an SEI enriched with Na_3P components was formed on the surface. The final full cell assembled with HC-3 wt% P matched with the cathode exhibited excellent rate performance, with a reversible discharge capacity of 78 mAh g^{-1} at 10 C, significantly exceeding the performance of recently reported bamboo powder-based hard carbon. The assembled pouch cell maintained stable cycling for 1000 cycles at 0.5 C. This work provides guidance from the perspective of SEI regulation and design for enhancing the fast-charging performance of biomass-derived hard carbon anodes in sodium-ion batteries.

Received 21st June 2025
Accepted 29th July 2025

DOI: 10.1039/d5sc04575d

rsc.li/chemical-science

Introduction

As the global energy transition proceeds and the search continues for greener sources of energy, the renewable energy generation and electric vehicle industries are experiencing rapid growth, leading to an increasing demand for large-scale energy storage technologies.[1,2] Sodium-ion batteries have emerged as one of the strongest candidates for next-generation energy storage systems due to the abundant resources for their production, low cost, and environmental friendliness.[3,4] Nevertheless, the commercialization of sodium-ion batteries is still fraught with numerous challenges, among which the performance limitations of the anode materials are particularly prominent. Hard carbon (HC) materials are advantageous because of their low cost, high sodium storage capacity, and satisfactory cycling stability, and a significant amount of research has been conducted in the study of anode materials for sodium-ion batteries.[5,6]

In recent years, there has been immense potential for biomass-derived hard carbon materials to serve as anode materials for sodium-ion batteries, primarily because of their abundant availability, renewability, and tunable structure.[7,8] Biomass precursors, such as lignin and cellulose, possess rich natural porous structures and heteroatoms (*e.g.*, oxygen and nitrogen), which, after carbonization, can form hard carbon materials with distinctive microstructures and surface chemical properties.[9,10] However, for fast-charging applications, a myriad of challenges remain for biomass-derived hard carbon materials.

For instance, the diversity of biomass precursors leads to significant structural variations in the carbonized products, and thus, it is difficult to precisely control performance.[11,12] Additionally, because the intrinsic conductivity of hard carbon materials is low, their electrochemical performance at high rates is limited.[13,14] Furthermore, side reactions between the hard carbon surface and the electrolyte can also compromise their cycling stability and fast-charging capabilities.[15,16] Therefore, enhancement of the fast-charging performance of biomass-derived hard carbon anodes through rational structural design and surface modification strategies has become a critical issue that needs to be addressed in current research.

[a]*School of Chemical Engineering and Technology, Xi'an Jiaotong University, Xi'an 710049, China. E-mail: tangw2018@xjtu.edu.cn*

[b]*National Innovation Platform (Center) for Industry-Education Integration of Energy Storage Technology, Xi'an Jiaotong University, Xi'an 710049, China*

[c]*College of Materials Science and Engineering, Sichuan University, Chengdu 610064, China. E-mail: zhangqianyu@scu.edu.cn*

[d]*School of Materials Science and Engineering, Anhui University, Hefei 230601, China. E-mail: cfz@ahu.edu.cn*

Recent studies on biomass-derived hard carbon and rapid charging of graphite anodes have provided valuable insights that can be leveraged to enhance the fast-charging performance of biomass-derived hard carbon anodes. Chen *et al.*[17] exposed the free radicals in natural bamboo by appropriate lignin removal, and the abundant free radicals facilitated the utilization of precursor fragments during the carbonization process, leading to the formation of a developed carbon layer with a substantial amount of closed pores. This structural characteristic enabled the hard carbon to achieve an optimal reversible capacity of 350 mAh g^{-1} under a current density of 20 mA g^{-1}. However, its reversible capacity significantly decayed to only 60 mAh g^{-1} when subjected to a high current density of 1000 mA g^{-1}.

Although the removal of lignin alone proved beneficial for the initial reversible capacity of bamboo-based hard carbon, the rate capability of this material did not meet the requirements for fast-charging anodes. Notably, Sun *et al.*[18] proposed that the solid electrolyte interphase (SEI) components play an important role in the desolvation of alkali metal ions during fast charging. Their findings revealed that SEI materials with higher Li^+ adsorption energy were capable of achieving faster desolvation processes. By constructing an ultrathin phosphorous layer on the graphite surface, they orchestrated an *in situ* transformation to a crystalline Li_3P-based SEI with high ionic conductivity.

Drawing inspiration from research on interfacial construction for fast-charging anodes, we designed the ideal SEI for fast-charging anodes to be thin with high Na^+ conductivity, which supports the rapid transport of Na^+ at the electrode surface. Herein, following the sublimation of red phosphorus and subsequent deposition upon cooling, a phosphide layer was constructed on the surface of the hard carbon derived from delignified bamboo powder as a precursor. During charge–discharge cycling, an SEI rich in Na_3P components was formed on the surface, while a solvation sheath with a low solvent coordination number formed near the inner Helmholtz plane (IHP) at the Na_3P interface, thereby supporting rapid Na^+ desolvation.

By inhibiting the continuous reduction of the electrolyte at the anode surface, a thinner and more homogeneous SEI layer was generated, resulting in a full cell composed of an O3–$NaNi_{1/3}Fe_{1/3}Mn_{1/3}O_2$ cathode. Consequently, this O3–$NaNi_{1/3}Fe_{1/3}Mn_{1/3}O_2$//3 wt% P HC full cell exhibited excellent rate performance, with a reversible discharge capacity of 78 mAh g^{-1} at 10 C, significantly outperforming recently reported bamboo powder-based hard carbon. Moreover, the assembled pouch cell maintained stable cycling for 1000 cycles at 0.5 C, demonstrating the feasibility of this method for the commercial application of hard carbon anodes.

Results and discussion

The phosphide layer of bamboo powder-based hard carbon is formed through the sublimation deposition of red phosphorus, as illustrated in Fig. 1a. During the charge–discharge process, an SEI enriched with Na_3P components is generated, which contributes to the hard carbon anode's superior electrochemical performance.[19] Fig. 1b compares the X-ray diffraction (XRD) results of the original bamboo powder-based hard carbon and hard carbon composites with varying mass percentages of red phosphorus. All samples exhibit two broad peaks at approximately 23° and 44°, corresponding to the 002 and 100 crystal planes of graphite, respectively, indicating that the samples retained the typical amorphous structure of hard carbon.[20] Moreover, the (002) peak shifts to a lower angle with increasing red phosphorus content, indicating that phosphidation enlarges the interlayer spacing of the graphite domains within the hard carbon.

Furthermore, the N_2 adsorption–desorption isotherms (Fig. 1c and S1, SI) show that the specific surface area of the red P/hard carbon composites is significantly smaller than that of the original hard carbon (original hard carbon: 23.2 m^2 g^{-1}; 1 wt% P, 3 wt% P, and 5 wt% P phosphated hard carbon: 6.73, 4.46, and 2.53 m^2 g^{-1}, respectively). Pore size analysis of the samples, conducted using the Barrett–Joyner–Halenda (BJH) method as shown in Table S1, indicates that the average pore size of the phosphated hard carbon is approximately 1.5 nm, which is smaller than that of the original hard carbon (3.7 nm).[21,22] The reduction in specific surface area and average pore size indicates that red phosphorus was successfully deposited on the surface of hard carbon, partially occluding its pores.

According to the X-ray photoelectron spectroscopy (XPS) shown in Fig. S4 (SI), the phosphated hard carbon exhibits a characteristic peak of P at approximately 130 eV compared to the original hard carbon. A detailed analysis of the high-resolution P 2p spectrum reveals peaks centered at 130 and 130.7 eV, corresponding to P $2p_{3/2}$ and P $2p_{1/2}$, respectively. Additionally, peaks at 131.6 and 134.3 eV were attributed to P–C and P–O–C bonds, respectively. These findings suggest that red phosphorus successfully forms a composite with hard carbon through robust chemical interactions.[23]

Small-angle X-ray scattering (SAXS) was further employed to analyze the closed pore characteristics that were not detectable by N_2 adsorption, as shown in Fig. S2 (SI). A plateau in the intensity variation was observed at 0.1 $Å^{-1}$, which was attributed to the presence of closed pores within the carbon structure.[24,25] In this region, the scattering intensity of the original hard carbon is notably higher than that of the 3 wt% P-HC, indicating that the original hard carbon contains additional closed pores. These closed pores facilitate the intercalation and insertion of sodium ions, contributing to sodium storage within the plateau region of the electrochemical profile. However, this structural feature is disadvantageous for rapid sodium storage kinetics,[26] while partial embedding of phosphorus into the carbon framework enlarges the interlayer spacing and decreases the number of stacked closed pores, thereby increasing rapid sodium storage.[27]

Compared to the original hard carbon (Fig. S5a, SI), the transmission electron microscopy (TEM) images and corresponding elemental mapping (Fig. 1e) of the 3 wt% P-HC further corroborate the uniform distribution of phosphorus on the surface of the hard carbon. Scanning electron microscopy (SEM) images (Fig. S6, SI) reveal that irregular block-like shapes were observed for all the hard carbon morphologies,

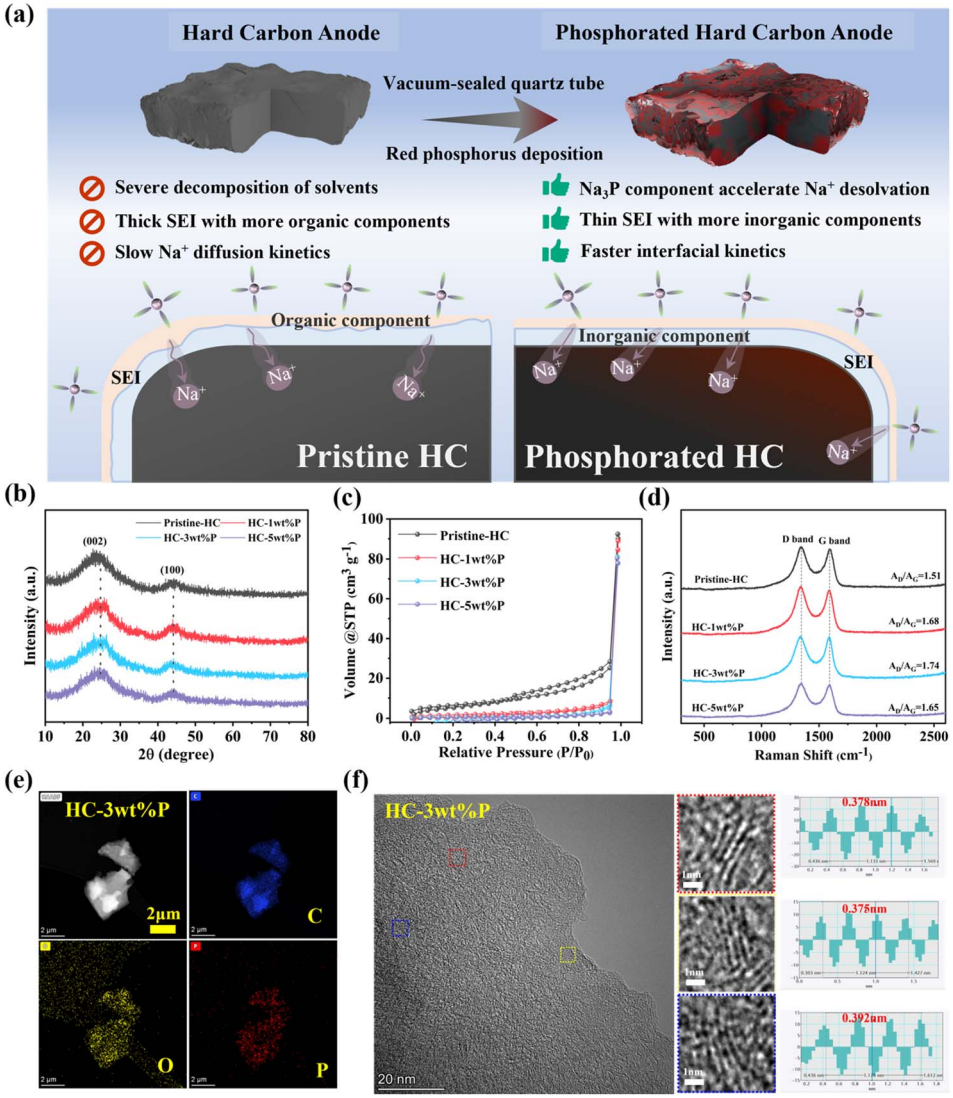

Fig. 1 Synthesis and structural features. (a) Schematic diagram showing the preparation of a phosphorated hard carbon anode and working mechanism of the phosphating layer design. (b) XRD patterns of all as-prepared samples. (c) N_2 adsorption–desorption isotherms. (d) Raman spectra. (e) HAADF-TEM images and element mapping of C, O, and P of HC-3 wt% P. (f) HRTEM images of HC-3 wt% P.

with the distribution of red phosphorus in the 5 wt% P-HC showing some degree of aggregation and unevenness. Further analysis of the graphite crystallite structure before and after phosphidation using high-resolution transmission electron microscopy (HRTEM) illustrates that the interlayer spacing of graphite crystallites in 3 wt% P-HC (0.375–0.392 nm) is larger than that of the original hard carbon (0.356–0.378 nm) (Fig. 1f and S5b, SI). This indicates that the bonding of red phosphorus with hard carbon has expanded the interlayer spacing of graphite crystallites, which is beneficial for the rapid insertion and extraction of Na^+ in phosphated hard carbon.[28,29]

Fig. 1d depicts the Raman spectra of several hard carbon samples, and Fig. S3 (SI) illustrates the peak-fitting results. By calculating the peak area ratio of the D band at 1350 cm^{-1} and the G band at 1570 cm^{-1} in the Raman spectra of the HC samples (Fig. 1d and S3, SI), it is evident that the AD/AG ratio increases in the phosphated anodes compared to the original hard carbon. This observation indicates that red phosphorus penetrates the carbon framework, thereby enhancing the degree of amorphization and introducing point defects within the structure.[30]

By integrating molecular dynamics (MD) simulations with density functional theory (DFT), we investigated the effects of conventional SEI components (including organic constituents, Na_2O, Na_2CO_3 and NaF) as well as Na_3P on the Na^+ solvation structure at the electrode–electrolyte interface. The findings further unveil the primary reasons for the enhanced Na^+ transport kinetics observed in biomass-derived hard carbon featuring a phosphated layer. Fig. 2a and S8 depict the utilization of MD simulations to compare Na_3P with conventional SEI components, including organic components (sodium ethylene monocarbonate (NEMC)) and inorganic components (Na_2O, Na_2CO_3 and NaF), in terms of their influence on the Na^+ solvation structure at the anode interface.[31–33]

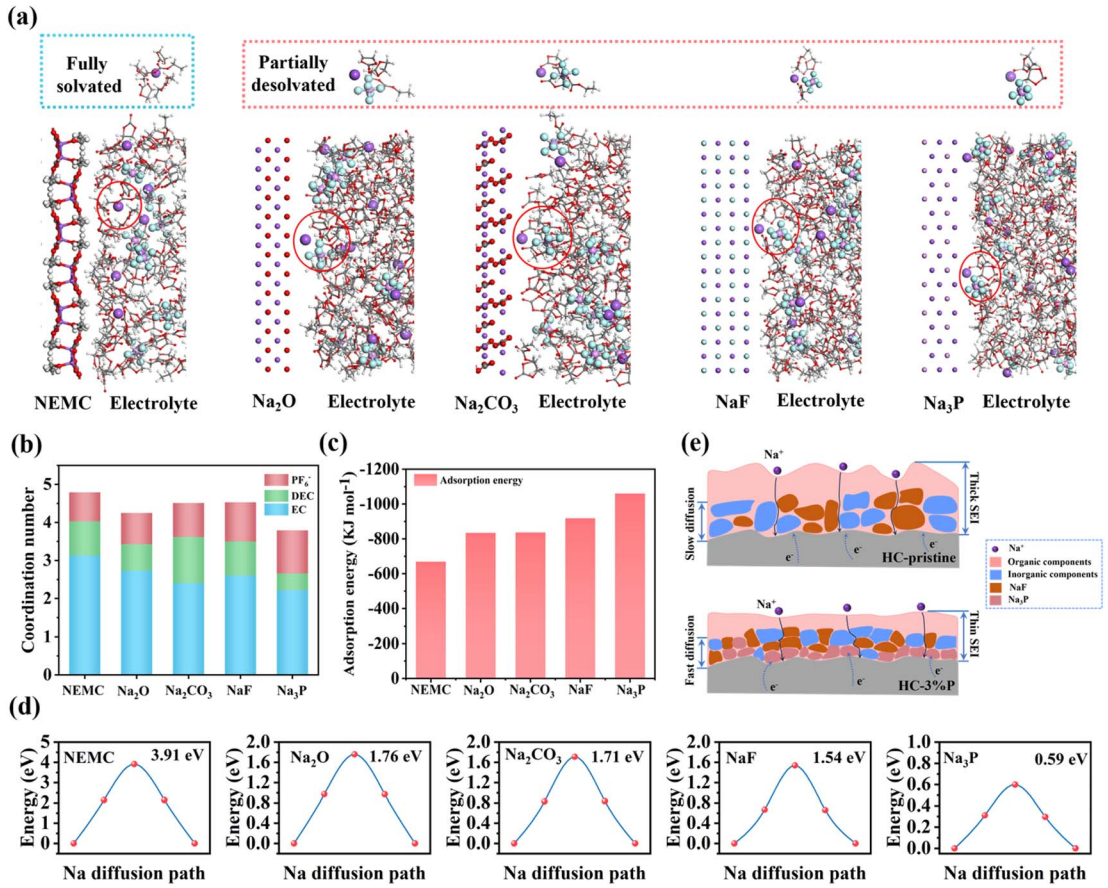

Fig. 2 The theoretical investigation of the desolvation process of Na^+ within (a) NEMC, Na_2O, Na_2CO_3, NaF and Na_3P based SEIs. (b) Coordination number of the solvation structure near the IHP on various SEI species based on the MD simulation results. (c) The adsorption energy of various SEI components for Na^+. (d) The Na^+ transfer energy barrier on the NEMC (100), Na_2O (111), Na_2CO_3 (101), NaF (111), and Na_3P (101) surfaces. (e) Schematic diagram of Na^+ across through different anodes SEI.

Based on the computed radial distribution function, the Na^+ solvation structures near the IHP were analyzed (as shown in Fig. 2b and S9, SI).[34,35] For the Na^+–O (ethylene carbonate (EC)/diethyl carbonate (DEC)) and Na^+–P (PF_6^-) pairs, the primary peaks of g(r) appear at 2.4 Å and 3.2 Å, respectively. Among all SEI components, EC exhibits a significantly higher coordination number than that of DEC and PF_6^-. Among all these solvated interfacial systems, Na^+ undergoes partial desolvation on the Na_3P surface, exhibiting the lowest coordination number of 3.79 Na^+, with lower solvent coordination being more prone to desolvation before diffusing through the SEI.[36,37] On the interface of organic component NEMC, Na^+ is almost entirely solvated by approximately 3.13 EC molecules and 0.9 DEC molecules, with the lowest number of PF_6^- ions (0.76) in the solvation shell. Furthermore, compared to NEMC, Na^+ exhibits an even lower coordination number on the surfaces of Na_2O, Na_2CO_3, and NaF.

Fig. 2c presents the density functional theory (DFT) calculations of Na^+ adsorption behavior on different SEI components (Fig. S7, SI). Na_3P exhibits the strongest adsorption energy for Na^+, resulting in distinct Na^+ solvation structures near the IHP at the anode interface. The calculations reveal that Na^+ can easily undergo desolvation on the Na_3P surface.[38,39] Furthermore, as shown in Fig. 2d and S10 (SI), the diffusion energy barriers of Na^+ on different SEI component crystal facets were computed and analyzed.

An exceptionally low Na^+ diffusion energy barrier of only 0.59 eV was observed on the Na_3P (101) surface. In contrast, Na^+ diffusion on the NEMC (100) surface requires a significantly higher energy barrier of 3.91 eV (Fig. 2d). To more clearly understand the effects of different SEI components on the solvation structure and sodium ion transport kinetics, the summary data are shown in Table S2. Combining the above MD and DFT calculation results, the construction of a phosphide layer, as illustrated in Fig. 2e, facilitates Na^+ desolvation, reduces continuous electrolyte consumption, and leads to the formation of a thinner SEI enriched with inorganic components.[40–42]

To elucidate the practical role of phosphorization treatment in enhancing the electrochemical performance of bamboo powder-derived hard carbon anodes, half-cells using different hard carbon materials as the working electrode and sodium metal as the counter and reference electrodes were employed for electrochemical characterizations. First, the HC-3 wt% P anode exhibited a contact angle of 11.3° with the electrolyte (commercial 1 M $NaPF_6$ in EC/DEC (v/v = 1 : 1)) (Fig. 3a), which

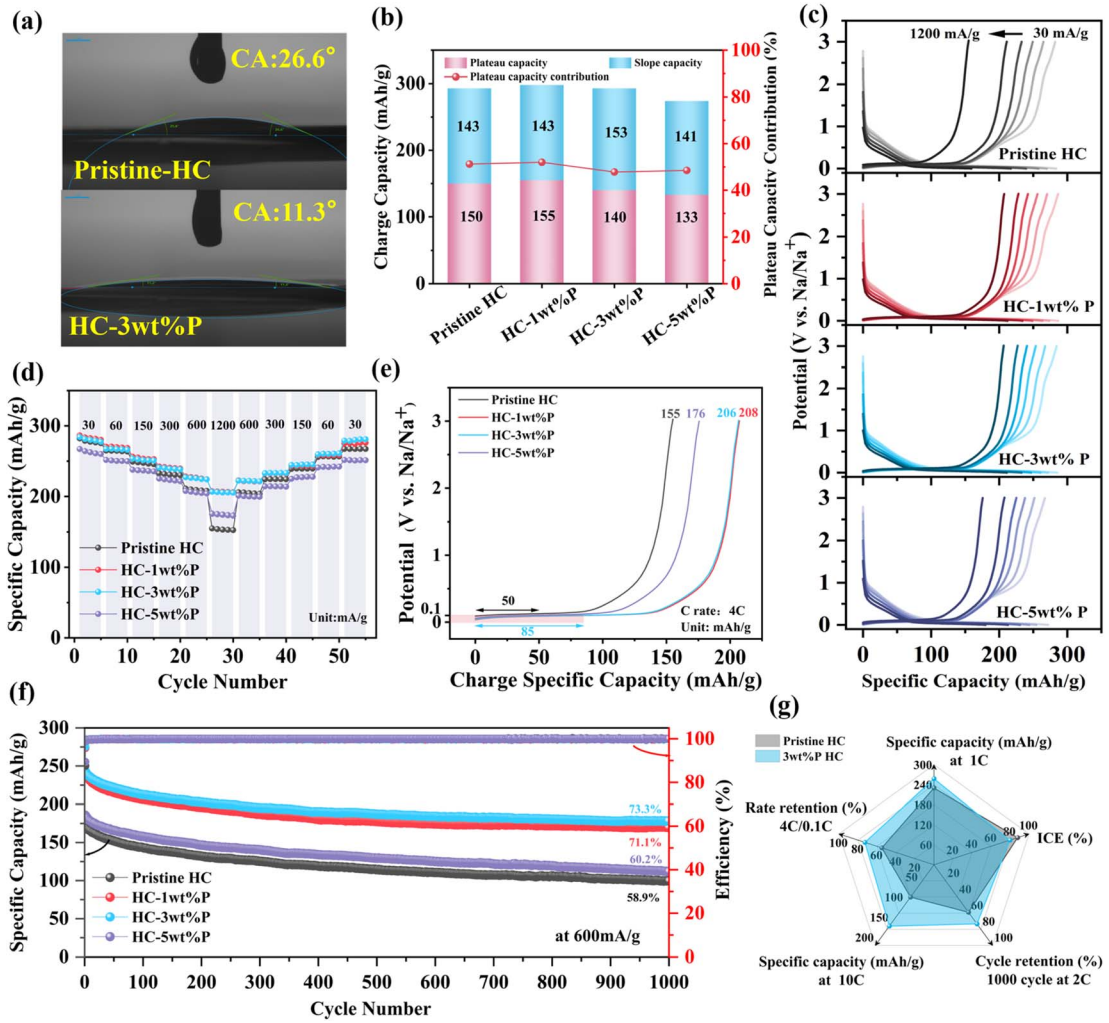

Fig. 3 Electrochemical performance of the phosphatized HC anodes. (a) Apparent contact angle between the electrode material and electrolyte. (b) Comparison between the sloping capacity and plateau capacity of samples based on the second charge curves at 30 mA g^{-1}. (c) The GCD curves of samples at current densities of 30–1200 mA g^{-1}. (d) Rate performance. (e) The charge curves for each sample at 4 C (1 C = 300 mA g^{-1}). (f) Long-term cycling stabilities at 600 mA g^{-1}. (g) Radar plot evaluating the electrochemical properties of the pristine-HC and 3 wt% P HC electrodes.

was significantly lower than that of pristine-HC (26.6°), suggesting enhanced wettability, which expands the electrode/electrolyte contact area and reduces the interfacial charge transfer impedance. In addition, more uniform electrolyte infiltration promotes the growth of a dense SEI in the first cycle, effectively inhibiting side reactions and interface instability. Moreover, the initial charge–discharge curves at 0.1 C (Fig. S11, SI) indicate that with increasing phosphorization content, the initial discharge capacity increases, which should be attributed to the reaction between sodium metal and the phosphide layer, forming Na_3P components in the SEI. Despite a marginal reduction in the initial coulombic efficiency (ICE), the HC-3 wt% P anode (ICE = 82%, 293 mAh g^{-1}) retained a reversible capacity nearly comparable to that of the pristine-HC anode (ICE = 88%, 291 mAh g^{-1}).

Further analysis of the second-cycle charging process (Fig. 3b) revealed that with an escalating phosphorization content, the contribution of reversible capacity in the high-voltage sloping region (relative to Na^+/Na > 0.1 V) increases.[43,44] The HC-3 wt% P anode exhibited the highest sloping-region capacity contribution at 52.2%, compared to 48.5% for the pristine-HC anode. Because the enhancement of capacity in the sloping region facilitated rapid sodium storage, the phosphorized hard carbon exhibited a superior rate performance (Fig. 3c and d) in comparison to pristine-HC. At current densities of 30, 60, 150, 300, 600, and 1200 mA g^{-1}, the HC-3 wt% P anode maintained relatively high capacities of 286, 270, 256, 242, 228, and 206 mAh g^{-1}, respectively, with the capacity retention from 0.1 C to 4 C rate testing also increasing from 54.9% for pristine-HC to 72.7% (Fig. S12a, SI).

The poor reversibility of pristine-HC during rate cycling tests may be attributed to continuous electrolyte decomposition caused by an unstable SEI. The galvanostatic charge–discharge (GCD) curves at a high rate (4 C) further indicate that the

phosphorized anode delivered a higher reversible capacity (Fig. 3e), particularly in the high-voltage region (relative to Na^+/Na > 0.1 V), where the capacity increased from 105 mAh g^{-1} (pristine-HC) to 121 mAh g^{-1} (HC-3 wt% P). This suggests that phosphorization enhances the high-voltage reversible adsorption of bamboo powder-derived hard carbon, thereby facilitating rapid Na^+ transport kinetics.

As for the cyclability shown in Fig. S12b (SI), the HC-3 wt% P anode maintained the highest charge-specific capacity of 223 mAh g^{-1} and a high capacity retention of 87.9% after 450 cycles at a current density of 300 mA g^{-1}. At an elevated current density of 600 mA g^{-1}, the charge–discharge cycling stability exhibited progressive enhancement with an increase in the red phosphorus content, as illustrated in Fig. 3f. After undergoing 1000 cycles, the HC-3 wt% P anode demonstrated the highest specific capacity of 178 mAh g^{-1}, accompanied by a retention rate of 73.3%. This represents a notable improvement when compared to the pristine-HC anode, which exhibited a specific capacity of 100 mAh g^{-1} and a retention rate of 58.9%.

Even when subjected to an ultra-high current density of 3 A g^{-1}, the HC-3 wt% P anode displayed superior stability and specific capacity over the course of 450 cycles, significantly surpassing the performance of the pristine-HC anode (refer to Fig. S12c in the SI). Furthermore, when evaluated at high current rates, the charge–discharge performance of the HC-3 wt% P anode displayed exceptional cycling stability in comparison to recently reported HC anodes (refer to Fig. S13 and Table S3 in the SI). The notable enhancement in cycling stability at high current rates is likely attributable to the initial formation of a more stable interface within the phosphorized hard-carbon anode (a detailed exploration of this phenomenon is provided in the subsequent sections), which was further coupled with a decrease in irreversible side reactions with the electrolyte.

The surface morphology of the hard carbon anode after 10 cycles was scrutinized using SEM and atomic force microscopy (AFM). Fig. 4a and c present a pristine-HC anode that exhibits significant agglomeration and pronounced surface roughness before and after cycling, whereas the HC-3 wt% P anode largely retained its original morphology after cycling. The magnified SEM images (Fig. S14, SI) further reveal fewer surface deposits and a smoother surface for the HC-3 wt% P anode. More localized and precise AFM images, as depicted in Fig. 4b and d reveal that, in contrast to the rough and uneven surface of the pristine-HC anode, the HC-3 wt% P anode developed a much smoother surface after cycling, which is consistent with the aforementioned observations.

Based on the observed differences in surface morphology, it can be speculated that compared to pristine hard carbon, the phosphorized hard carbon anode can mitigate side reactions of the electrolyte and suppress its continuous degradation, thereby forming a thinner SEI. The microstructure of the SEI was further observed through TEM. As shown in Fig. 5a, compared to the SEI on the pristine-HC electrode, which exhibited an uneven thickness (28–50 nm), the SEI observed on the HC-3 wt% P electrode was thinner and more uniform (15–22 nm).

Further XPS with varying etching depths was conducted to investigate the structure and composition of the SEI on the HC anode after 10 cycles. By fitting detailed XPS peaks and binding energies, it was determined that while the SEI composition was similar across the samples, the content of its various components varied (Table S4, SI). Fig. 4e and f (Fig. S16, SI) present the high-resolution spectra of C 1s, O 1s, F 1s, P 2p, and Na 1s for the pristine-HC and HC-3 wt% P anodes after cycling. In the C 1s spectrum, peaks appeared at 284.7 eV (C–C), 286.1 eV (C–O), and 286.7 eV (COO), while the O 1s peak at 533.8 eV (C–O/O–H) corresponded to organic components such as $ROCO_2Na$ and $(CH_2OCO_2Na)_2$, which are generated from solvent decomposition. The C 1s peak at 289.7 eV (CO_3), the O 1s peak at 531.5 eV (Na–O), and the F 1s peak at 685.5 eV (Na–F) were attributed to the inorganic components Na_2CO_3, Na_2O, and NaF, respectively.[42,45]

As the sputtering depth increased, the proportion of inorganic components in the SEI on the HC-3 wt% P anode was generally higher than that in the SEI on the pristine-HC anode (Fig. 4g), indicating that the presence of the phosphorization layer facilitated the formation of an SEI rich in inorganic components on the anode surface. Such a structure not only exhibited greater stability, but also assisted in reducing the continuous consumption of the electrolyte.[18,19] Furthermore, a higher proportion of inorganic components in the SEI enhanced the conductivity of Na^+, which is crucial for the significantly enhanced rate performance of the HC-3 wt% P anode.

Time-of-flight secondary ion mass spectrometry (TOF-SIMS) was utilized to more qualitatively analyze the compositional distribution within the SEI. As shown in Fig. 4h, i, S17, and S18 (SI), ion fragments corresponding to relevant inorganic components, including NaF^-, NaP^-, $NaCO_3^-$, and NaO^- were detected. Additionally, the $C_2H_2O^-$ fragment was attributed to organic compounds.[46] The NaP^- fragment content was consistently higher across the surface of the HC-3 wt% P anode compared to the pristine-HC anode (Fig. 4j). This was associated with the preferential formation of Na_3P during the initial discharge stage due to the interaction between the phosphorization layer and sodium metal. Additionally, the NaF^- fragment also exhibited a higher concentration on the surface of the HC-3 wt% P anode. In contrast, the $C_2H_2O^-$ fragment was primarily concentrated on the surface of the HC-3 wt% P anode, with a significantly reduced presence at greater depths.

The quantitative statistical results from the 3D visual maps indicated that for the cycled phosphorized anode, inorganic components were abundant and dominated the entire SEI, while organic components were present in lower amounts and were mainly distributed on the outer surface of the SEI. The combination of a thinner, inorganic-rich, and chemically uniform SEI facilitated the formation of a homogeneous Na^+ diffusion channel on the HC anode surface.[35,40] EDS mapping further confirmed that there was greater uniformity in the distribution of Na in the cycled phosphorized anode (Fig. S19, SI).

The inorganic-rich and thinner SEI structure impacted the kinetics of sodium ion transport and storage. Based on electrochemical impedance spectroscopy (EIS) measurements

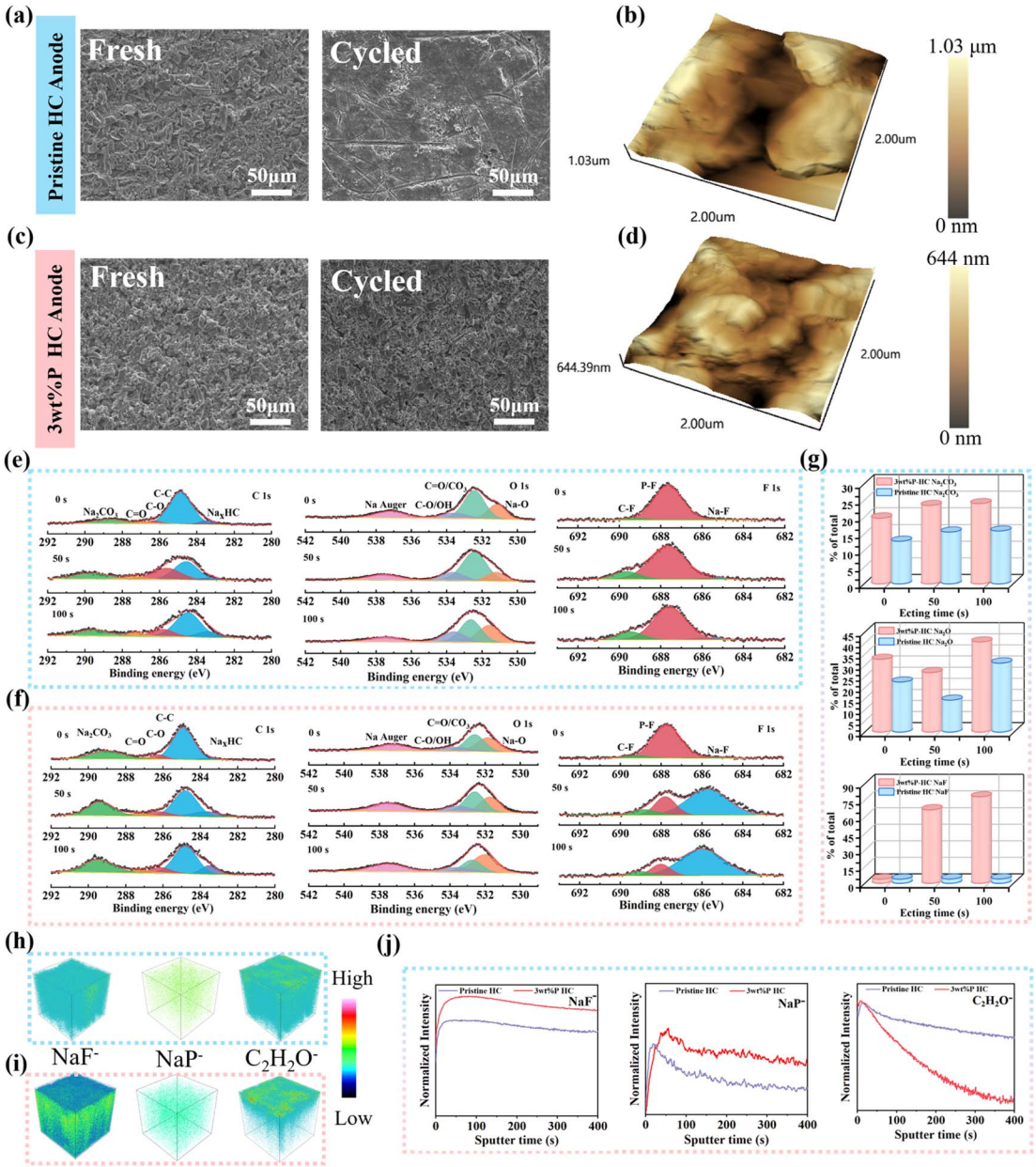

Fig. 4 Characterization of SEI properties of the phosphatized HC and pristine-HC anodes. (a and b) SEM and 3D topographical AFM images of fresh and cycled pristine-HC anodes. (c and d) SEM and 3D topographical AFM images of fresh and cycled 3 wt% P HC anodes. (e and f) Depth-profiling XPS spectra of C 1s, O 1s, and F 1s from the pristine-HC and phosphatized HC anodes, respectively. (g) The proportion of SEI components calculated from the C 1s, O 1s, and F 1s spectra. (h and i) 3D distributions of secondary ion fragments from various species obtained by sputtering and TOF-SIMS analysis of the pristine-HC and phosphatized HC anodes, respectively. (j) The corresponding ionic distributions along the depth profiles.

(Fig. 5b and S20, SI), the HC-3 wt% P anode exhibited the smallest charge transfer resistance (R_{ct}). The as-calculated Warburg factor (σ) value for HC-3 wt% P (32.9) was significantly lower than that for pristine-HC (69.3), indicating superior electrochemical kinetics.[47]

Temperature-dependent EIS measurements were conducted to obtain the Na^+ transport and charge transfer resistances across the SEI, and the apparent activation energy for Na^+ transport was calculated using the Arrhenius law (eqn (1)):[48]

$$\sigma T = A \exp(-E_a/k_B T) \quad (1)$$

where k denotes the reaction rate constant, A denotes the pre-exponential factor, R represents the molar gas constant, and T denotes the absolute temperature. The activation energy for Na^+ transport across the SEI and charge transfer at the HC-3 wt% P anode (Fig. 5c) is 47.31 kJ mol^{-1}, which was lower than that for the pristine-HC anode (59.94 kJ mol^{-1}), indicating that the Na^+ diffusion kinetics at the interface and within the SEI were improved on the phosphated anode surface.

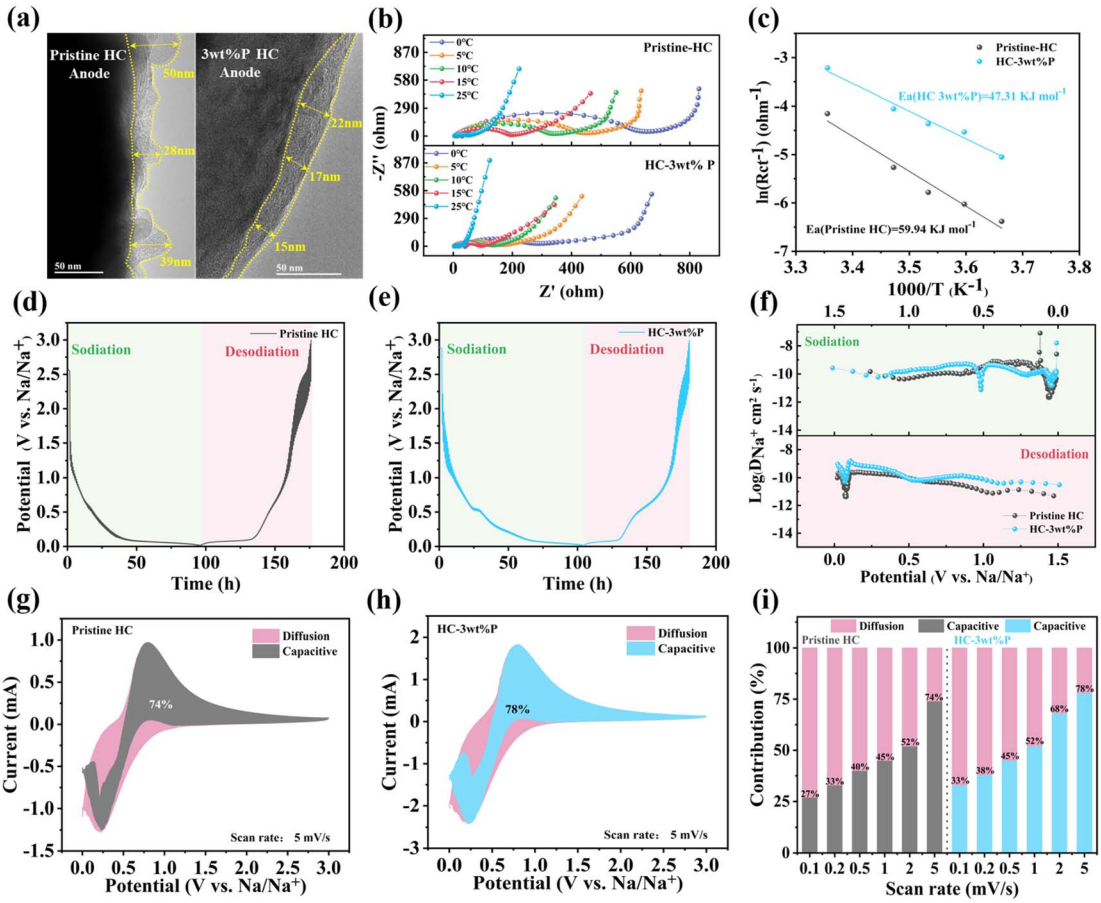

Fig. 5 Electrode kinetic analysis of the phosphatized HC and pristine-HC anodes. (a) HRTEM images of cycled anodes. (b) Temperature-dependent Nyquist plots of pristine-HC and 3 wt% P HC electrodes from 273 K to 298 K. (c) The activation energies for the charge-transfer process. (d and e) GITT curves of pristine-HC and phosphatized HC anodes, respectively. (f) The diffusion coefficients of Na^+ calculated from the GITT curves. (g and h) The capacitive and diffusion contribution at 5 mV s^{-1} of the pristine-HC and phosphatized HC anodes. (i) Capacitive contributions at various scanning rates.

Furthermore, according to the galvanostatic intermittent titration technique (GITT) tests (Fig. 5d, e and S21, SI), the Na^+ diffusion coefficient for the HC-3 wt% P anode was higher compared to the pristine-HC anode (Fig. 5f), which was attributed to the enhanced electrode–electrolyte affinity as well as the as-formed inorganic-rich SEI originated from the well-designed phosphating layer.

A kinetic analysis of the fast-charging performance improvement in the half-cell was conducted through varying scan rate cyclic voltammetry (CV) tests. Analysis of the CV curves for the first three cycles at a scan rate of 0.1 mV s^{-1} (Fig. S22, SI) revealed that the area enclosed by the phosphated anode's curves was generally larger, indicating that additional Na^+ undergoes reversible migration during the charge–discharge process. This further supports the higher reversible capacity observed in the previous GCD tests.

Pseudocapacitive current contributions were fitted using surface-controlled and diffusion-controlled formulas (Fig. S23, SI) based on CV curves obtained at scan rates of 0.1, 0.2, 0.5, 1, 2, and 5 mV s^{-1}.[49] As shown in Fig. 5g and h, the capacitive contribution significantly increased with the scan rate. At a scan rate of 5 mV s^{-1}, the capacitive current contribution of the HC-3 wt% P anode was 78%, which was higher than that of the pristine-HC anode at 74% (Fig. 5i). These results confirmed that during high-rate charge/discharge processes, the HC-3 wt% P anode exhibited superior fast sodium storage kinetics.

To assess the commercialization prospects of the phosphated bamboo powder-based hard carbon anode, sodium-ion full cells were assembled with pristine-HC and HC-3 wt% P as anodes and O3–$NaNi_{1/3}Fe_{1/3}Mn_{1/3}O_2$ (NNFM) as the cathode for electrochemical testing. As shown in Fig. S24 (SI), the full cell provided a high reversible capacity of 125 mAh g^{-1} within a current rate of 0.1 C and a voltage window of 1.5–3.9 V (1 C = 150 mA g^{-1}).[50]

Fig. 6a shows that the assembled full cell achieved a highly reversible rate performance (0.1 C–10 C–0.1 C). The HC-3 wt% P//NNFM full cell provided a reversible capacity of 78 mAh g^{-1} at a high rate of 10 C, which was significantly better than the 10 C performance (45 mAh g^{-1}) of the pristine-HC//NNFM full cell. Fig. 6b and c reveal that during high current charge/discharge, the pristine-HC//NNFM full cell experienced significant electrochemical polarization, leading to a substantial capacity

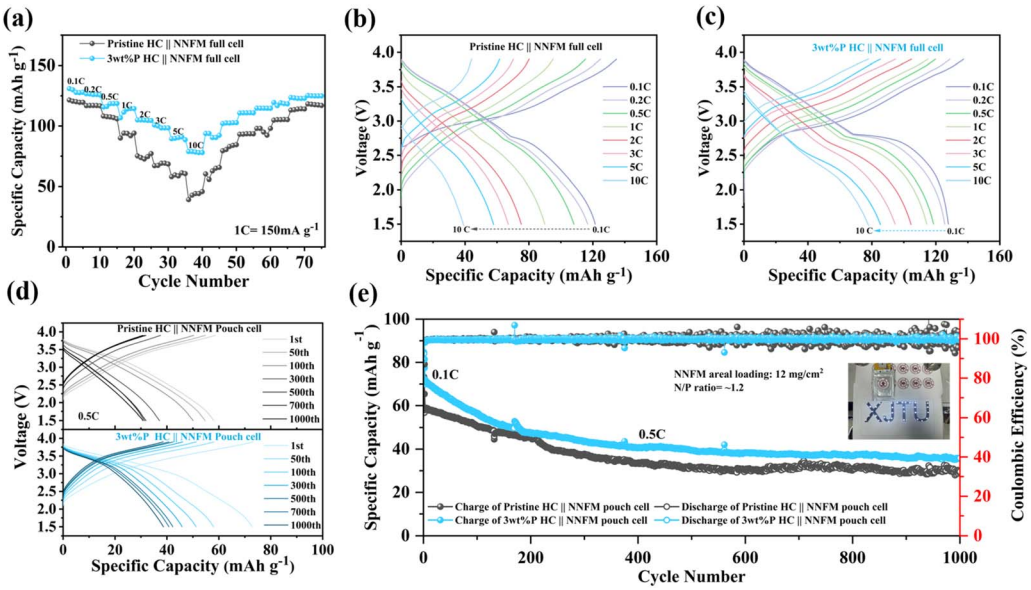

Fig. 6 Electrochemical performance of 3 wt% P HC and pristine-HC//NNFM full cell. (a) Rate capability. (b and c) At different current densities, the GCD profiles of the pristine-HC and 3 wt% P HC//NNFM full cells, respectively. (d) GCD curves of the pristine-HC and 3 wt% P HC//NNFM pouch cells during the different cycles at 0.5 C. (e) Long-term cycling stability of pouch cells at 0.5 C for 1000 cycles (the inset photograph shows a practical scene of lighting LED lamps with the pouch cell).

decay. After 100 cycles at 2 C, the HC-3 wt% P-assembled full cell maintained more stable charge/discharge behavior, with a capacity retention rate of 81.8% (Fig. S25a–c, SI).

Furthermore, pouch cells featured a high-loading cathode (approximately 12 mg cm^{-2}). Rate tests at 0.1 C–2 C also confirmed that the phosphated anode indeed improves the fast-charging performance of the pouch cell (Fig. S25d–f, SI). Long-cycle testing performed at a 0.5 C rate verified that the pouch cell incorporating the phosphated anode demonstrated more stable cycling behavior, and delivered a higher discharge capacity. The inset in Fig. 6d and e illustrates the pouch cell illuminating the XJTU logo. This demonstrates its potential for practical applications.

Conclusions

A strategy is proposed herein to enhance the fast-charging performance of bamboo-derived hard carbon by constructing a phosphating layer. The phosphating layer on the surface of bamboo-derived hard carbon can induce the formation of an SEI enriched in inorganic components such as Na_3P and NaF, which can effectively suppress continuous side reactions between the electrode and the electrolyte and reduce the impedance during charging and discharging to improve the efficiency of the battery. Moreover, Na_3P near the inner Helmholtz plane (IHP) can promote the formation of a solvation shell with a low solvent coordination number, and thus, the Na^+ desolvation capability as well as the conductivity can be strengthened accordingly. This facilitates the rapid storage capacity of sodium ions in high voltage regions (>0.1 V) to improve the rate performance.

Among the designed gradient-phosphated hard carbon anodes, the HC-3 wt% P anode exhibited the best Na^+ storage performance and excellent rate capability in half-cell performance tests. Furthermore, a pouch cell assembled with the corresponding cathode demonstrated stable cycling for 1000 cycles at 0.5 C. The construction of a phosphating layer on bamboo powder-based hard carbon proposed in this study provides meaningful guidance for rationally improving the SEI on the anode side to bridge the gap between interfacial chemistry and fast-charging performance.

Author contributions

Haihan Zhang: writing – original draft, methodology, investigation, data curation. Zhenxin Huang: software, investigation. Siyuan Lin: data curation, manuscript revision. Jiawu Cui: data curation, investigation. Qianyu Zhang: supervision. Xiansheng Luo: data curation. Rui Wang: data curation. Chaofeng Zhang: formal analysis. Chengyong Shu: supervision, project administration. Wei Tang: writing – review and editing, supervision, project administration, and funding acquisition.

Conflicts of interest

There are no conflicts to declare.

Data availability

The data underlying this study are available in the published article and its SI, or from the authors on request.

Additional data from the characterization of materials (pore size distribution; TEM images; long-term cyclic performance; CV curves; and comparison of electrochemical properties). See DOI: https://doi.org/10.1039/d5sc04575d.

Acknowledgements

This project was supported by the National Key R&D Program of China (2021YFB2400400), the National Natural Science Foundation of China (Grant No. 22379120 and 22278276), the Key Research and Development Plan of Shanxi Province (China, Grant No. 2018ZDXM-GY-135 and 2021JLM-36), the Higher Education Institution Academic Discipline Innovation and Talent Introduction Plan (”111 Plan”) (No. B23025), “Young Talent Support Plan” of Xi'an Jiaotong University (71211201010723), Sichuan Provincial Natural Science Foundation Outstanding Youth Science Fund (No. 2025NSFJQ0027), and Qingyuan City's 2023 Provincial Science and Technology Innovation Strategy Special Project (“Major Project + Task List”) (2023DZX015).

References

1 R. Usiskin, Y. Lu, J. Popovic, M. Law, P. Balaya, Y.-S. Hu and J. Maier, Fundamentals, status and promise of sodium-based batteries, *Nat. Rev. Mater.*, 2021, **6**, 1020–1035.
2 F. Wang, Z. Jiang, Y. Zhang, Y. Zhang, J. Li, H. Wang, Y. Jiang, G. Xing, H. Liu and Y. Tang, Revitalizing sodium-ion batteries *via* controllable microstructures and advanced electrolytes for hard carbon, *eScience*, 2024, **4**, 100181.
3 Y.-F. Sun, Y. Li, Y.-T. Gong, Z.-X. Qiu, J. Qian, Y. Bai, Z.-L. Wang, R.-P. Zhang and C. Wu, Constructing three-dimensional architectures to design advanced anodes materials for sodium-ion batteries: from nanoscale to microscale, *Energy Mater.*, 2024, **4**, 400002.
4 L. Liu, L. Xiao, Z. Sun, S. Bashir, R. Kasi, Y. Gu and R. Subramaniam, Rational manipulation of electrolyte to induce homogeneous SEI on hard carbon anode for sodium-ion battery, *J. Energy Chem.*, 2024, **94**, 414–429.
5 Y. Guo, S. Ji, F. Liu, Z. Zhu, J. Xiao, K. Liu, Y. Zhang, S. Liao and X. Zeng, A review of the preparation and characterization techniques for closed pores in hard carbon and their functions in sodium-ion batteries, *Energy Mater.*, 2025, **5**, 500030.
6 Y. Wan, B. Huang, W. Liu, D. Chao, Y. Wang and W. Li, Fast-Charging Anode Materials for Sodium-Ion Batteries, *Adv. Mater.*, 2024, **36**, 2404574.
7 B. Zhong, C. Liu, D. Xiong, J. Cai, J. Li, D. Li, Z. Cao, B. Song, W. Deng, H. Peng, H. Hou, G. Zou and X. Ji, Biomass-Derived Hard Carbon for Sodium-Ion Batteries: Basic Research and Industrial Application, *ACS Nano*, 2024, **18**, 16468–16488.
8 S. Zhou, Z. Tang, Z. Pan, Y. Huang, L. Zhao, X. Zhang, D. Sun, Y. Tang, A. S. Dhmees and H. Wang, Regulating closed pore structure enables significantly improved sodium storage for hard carbon pyrolyzing at relatively low temperature, *SusMat*, 2022, **2**, 357–367.
9 C. Wu, Y. Yang, Y. Zhang, H. Xu, W. Huang, X. He, Q. Chen, H. Dong, L. Li, X. Wu and S. Chou, Industrial-Scale Hard Carbon Designed to Regulate Electrochemical Polarization for Fast Sodium Storage, *Angew. Chem., Int. Ed.*, 2024, **63**, e202406889.
10 H. Zhang, M. Yang, Z. Xiao, K. Xie, L. Shao, C. Huang, C. Shu, C. Peng, Y. Wu and W. Tang, Flexible Precursor Modulation toward Selective Heteroatom Doping in a Hard-Carbon Anode for Sodium-Ion Batteries, *Energy Fuels*, 2023, **37**, 15127–15137.
11 J. Cui, P. Su, W. Li, X. Wang, Y. Zhang, Z. Xiao, Q. An and Z. Chen, Advanced Cellulose-Derived Hard Carbon as Anode for Sodium-Ion Batteries: Mechanisms, Optimization, and Challenges, *Adv. Energy Mater.*, 2025, **15**, 2404604.
12 T. Zhang, T. Zhang, C. Zhao, F. Wang, L. Zhang, Y. Li, L. Zhang and F. Ran, Revealing Effect of Aggregation Structure of Plant Precursors on Rate Performance of Carbon Anode for Sodium-Ion Batteries, *Adv. Funct. Mater.*, 2025, 2425234, DOI: 10.1002/adfm.202425234.
13 H. Zhang, S. Lin, C. Shu, Z. Tang, X. Wang, Y. Wu and W. Tang, Advances and perspectives of hard carbon anode modulated by defect/hetero elemental engineering for sodium ion batteries, *Mater. Today*, 2025, **85**, 231–252.
14 M. H. Song, Q. Song, T. Zhang, X. M. Huo, Z. Z. Lin, Z. W. Hu, L. Dong, T. Jin, C. Shen and K. Y. Xie, Growing curly graphene layer boosts hard carbon with superior sodium-ion storage, *Nano Res.*, 2023, **16**, 9299–9309.
15 Y. Li, Q. Zhou, S. Weng, F. Ding, X. Qi, J. Lu, Y. Li, X. Zhang, X. Rong, Y. Lu, X. Wang, R. Xiao, H. Li, X. Huang, L. Chen and Y.-S. Hu, Interfacial engineering to achieve an energy density of over 200 Wh kg^{-1} in sodium batteries, *Nat. Energy*, 2022, **7**, 511–519.
16 W. Kuang, X. Zhou, Z. Fan, X. Chen, Z. Yang, J. Chen, X. Shi, L. Li, R. Zeng, J.-Z. Wang and S. Chou, Sulfur-Containing Inorganic-Rich Interfacial Chemistry Empowers Advanced Sodium-Ion Full Batteries, *ACS Energy Lett.*, 2024, **9**, 4111–4118.
17 Y. Wang, Z. Yi, L. Xie, Y. Mao, W. Ji, Z. Liu, X. Wei, F. Su and C. M. Chen, Releasing Free Radicals in Precursor Triggers the Formation of Closed Pores in Hard Carbon for Sodium-Ion Batteries, *Adv. Mater.*, 2024, **36**, 2401249.
18 S. Tu, B. Zhang, Y. Zhang, Z. Chen, X. Wang, R. Zhan, Y. Ou, W. Wang, X. Liu, X. Duan, L. Wang and Y. Sun, Fast-charging capability of graphite-based lithium-ion batteries enabled by Li_3P-based crystalline solid–electrolyte interphase, *Nat. Energy*, 2023, **8**, 1365–1374.
19 Y. Liao, L. Yuan, Y. Han, C. Liang, Z. Li, Z. Li, W. Luo, D. Wang and Y. Huang, Pentafluoro(phenoxy) cyclotriphosphazene Stabilizes Electrode/Electrolyte Interfaces for Sodium-Ion Pouch Cells of 145 Wh Kg(−1), *Adv. Mater.*, 2024, **36**, e2312287.
20 S. You, Q. Zhang, J. Liu, Q. Deng, Z. Sun, D. Cao, T. Liu, K. Amine and C. Yang, Hard carbon with an opened pore structure for enhanced sodium storage performance, *Energy Environ. Sci.*, 2024, **17**, 8189–8197.

21 Y.-C. Tan, W.-W. Liu, W.-Y. Wang, X.-X. Liu, J.-M. Du and Y.-M. Sun, Embedment of red phosphorus in anthracite matrix for stable battery anode, *Rare Met.*, 2022, **41**, 2819–2825.

22 Y. Zeng, F. Wang, Y. Cheng, M. Chen, J. Hou, D. Yang, Y. Zhang, W. Yang, G. Liu, Y. Zhang, Z. Zhu, X. Li, Y. Yang and J. Zhao, Identifying the importance of functionalization evolution during pre-oxidation treatment in producing economical asphalt-derived hard carbon for Na-ion batteries, *Energy Storage Mater.*, 2024, **73**, 103808.

23 Z. G. Liu, J. Zhao, H. Yao, X. X. He, H. Zhang, Y. Qiao, X. Q. Wu, L. Li and S. L. Chou, P-doped spherical hard carbon with high initial coulombic efficiency and enhanced capacity for sodium ion batteries, *Chem. Sci.*, 2024, **15**, 8478–8487.

24 K.-Y. Zhang, H.-H. Liu, J.-M. Cao, J.-L. Yang, M.-Y. Su, X.-Y. Wang, Z.-Y. Gu, J. Wang, B. Li, Y. Wang and X.-L. Wu, Microstructure reconstruction *via* confined carbonization achieves highly available sodium ion diffusion channels in hard carbon, *Energy Storage Mater.*, 2024, **73**, 103839.

25 Q. Hu, L. Xu, G. Liu, J. Hu, X. Ji and Y. Wu, Understanding the Sodium Storage Behavior of Closed Pores/Carbonyl Groups in Hard Carbon, *ACS Nano*, 2024, **18**, 21491–21503.

26 Y. Fang, L. Li, J. Li, Y. Gan, J. Du, J. Li, X. Chen, H. Pan, W. Zhang, J. Gu, D. Zhang and Q. Liu, Ultrafast High-Volumetric Sodium-Ion Capacitors Based on Compact Nanoarchitectured Carbon Electrodes, *Adv. Funct. Mater.*, 2024, **34**, 2408568.

27 J. Peng, H. Wang, X. Shi and H. J. Fan, Ultrahigh Plateau-Capacity Sodium Storage by Plugging Open Pores, *Adv. Mater.*, 2024, 2410326.

28 Z. Huang, J. Huang, L. Zhong, W. Zhang and X. Qiu, Deconstruction Engineering of Lignocellulose Toward High-Plateau-Capacity Hard Carbon Anodes for Sodium-Ion Batteries, *Small*, 2024, **20**, 2405632.

29 Z. Zheng, S. Hu, W. Yin, J. Peng, R. Wang, J. Jin, B. He, Y. Gong, H. Wang and H. J. Fan, CO_2-Etching Creates Abundant Closed Pores in Hard Carbon for High-Plateau-Capacity Sodium Storage, *Adv. Energy Mater.*, 2023, **14**, 2303064.

30 J. Yan, H. Li, K. Wang, Q. Jin, C. Lai, R. Wang, S. Cao, J. Han, Z. Zhang, J. Su and K. Jiang, Ultrahigh Phosphorus Doping of Carbon for High-Rate Sodium Ion Batteries Anode, *Adv. Energy Mater.*, 2021, **11**, 2003911.

31 L. Wang, A. Menakath, F. Han, Y. Wang, P. Y. Zavalij, K. J. Gaskell, O. Borodin, D. Iuga, S. P. Brown, C. Wang, K. Xu and B. W. Eichhorn, Identifying the components of the solid–electrolyte interphase in Li-ion batteries, *Nat. Chem.*, 2019, **11**, 789–796.

32 C. Yang, W. Zhong, Y. Liu, Q. Deng, Q. Cheng, X. Liu and C. Yang, Regulating solid electrolyte interphase film on fluorine-doped hard carbon anode for sodium-ion battery, *Carbon Energy*, 2024, **6**, 503.

33 P. Liu, L. Miao, Z. Sun, X. Chen and L. Jiao, Sodiophilic Substrate Induces NaF-Rich Solid Electrolyte Interface for Dendrite-Free Sodium Metal Anode, *Adv. Mater.*, 2024, 2406058.

34 L. Chen, M. Chen, Q. Meng, J. Zhang, G. Feng, X. Ai, Y. Cao and Z. Chen, Reconstructing Helmholtz Plane Enables Robust F-Rich Interface for Long-Life and High-Safe Sodium-Ion Batteries, *Angew. Chem., Int. Ed.*, 2024, **63**, e202407717.

35 Y. H. Feng, M. Liu, W. Qi, H. Liu, Q. Liu, C. Yang, Y. Tang, X. Zhu, S. Sun, Y. M. Li, T. L. Chen, B. Xiao, X. Ji, Y. You and P. F. Wang, Dual-Anionic Coordination Manipulation Induces Phosphorus and Boron-Rich Gradient Interphase Towards Stable and Safe Sodium Metal Batteries, *Angew. Chem., Int. Ed.*, 2024, **64**, e202415644.

36 Z. Huang, Z. Xiao, H. Zhang, Q. Zhang, J. Cui, J. Luo, W. Tang and Y. Wu, Temperature-Robust Solvation Enabled by Solvent Interactions for Low-Temperature Sodium Metal Batteries, *J. Am. Chem. Soc.*, 2025, **147**, 5162–5171.

37 X. Hou, S. Wang, B. Wang, Y. Qiu, M. Jiang, Y. Tang, Q. Zheng and X. Li, Electrolyte Reconfiguration by Cation/Anion Cross-coordination for Highly Reversible and Facile Sodium Storage, *Angew. Chem., Int. Ed.*, 2024, **64**, e202416939.

38 Y. Liu, S. Yang, H. Guo, Z. Wang, J. Liu, N. Chen and X. Gong, Low LUMO energy carbon molecular interface to suppress electrolyte decomposition for fast charging natural graphite anode, *Energy Storage Mater.*, 2024, **73**, 103806.

39 S. Zhao and F. Huang, Weakly Solvating Few-Layer-Carbon Interface toward High Initial Coulombic Efficiency and Cyclability Hard Carbon Anodes, *ACS Nano*, 2024, **18**, 1733–1743.

40 S. Ma, J. Zhao, H. Xiao, Q. Gao, F. Li, C. Song and G. Li, Modulating the Inner Helmholtz Plane towards Stable Solid Electrolyte Interphase by Anion-π Interactions for High-Performance Anode-Free Lithium Metal Batteries, *Angew. Chem., Int. Ed.*, 2024, **64**, e202412955.

41 X. Liu, M. Zhang, X. Wang, Y. Peng, Y. Liu, S. Ullah, Z. Duan, W. Gao, B. Song, M. Wei, J. He, Z. Li and Y. Wu, Evidence of Quasi-Na Metallic Clusters in Sodium Ion Batteries through *In Situ* X-Ray Diffraction, *Adv. Mater.*, 2024, **37**, 2410673.

42 M. Liu, F. Wu, Y. Gong, Y. Li, Y. Li, X. Feng, Q. Li, C. Wu and Y. Bai, Interfacial Catalysis Enabled Layered and Inorganic-Rich SEI on Hard Carbon Anodes in Ester Electrolytes for Sodium-Ion Batteries, *Adv. Mater.*, 2023, **35**, e2300002.

43 Y. Aniskevich, J. H. Yu, J. Y. Kim, S. Komaba and S. T. Myung, Tracking Sodium Cluster Dynamics in Hard Carbon with a Low Specific Surface Area for Sodium-Ion Batteries, *Adv. Energy Mater.*, 2024, **14**, 2304300.

44 J. C. Hyun, H. M. Jin, J. H. Kwak, S. Ha, D. H. Kang, H. S. Kim, S. Kim, M. Park, C. Y. Kim, J. Yoon, J. S. Park, J.-Y. Kim, H.-D. Lim, S. Y. Cho, H.-J. Jin and Y. S. Yun, Design guidelines for a high-performance hard carbon anode in sodium ion batteries, *Energy Environ. Sci.*, 2024, **17**, 2856–2863.

45 H. Zhang, L. Song, S. Lin, Z. Huang, C. Shu, Y. Ma, Z. Tang, X. Wang, W. Tang and Y. Wu, Ameliorating the sodium storage performance of hard carbon anode through rational modulation of binder, *Energy Storage Mater.*, 2024, **73**, 103796.

46 Y. Dong, Y. Chen, X. Yue and Z. Liang, Unveiling the adsorption tendency of film-forming additives to enable fast-charging hard carbon anodes with regulated Li plating, *Energy Environ. Sci.*, 2024, **17**, 2500–2511.
47 Y. Zhao, Z. Hu, W. Zhou, P. Gao, Z. Liu, J. Liu, C. Fan and J. Liu, Advanced Structural Engineering Design for Tailored Microporous Structure *via* Adjustable Graphite Sheet Angle to Enhance Sodium-Ion Storage in Anthracite-Based Carbon Anode, *Adv. Funct. Mater.*, 2024, 2405174, DOI: **10.1002/adfm.202405174**.
48 Z. Y. Lu, H. J. Yang, Y. Guo, H. X. Lin, P. Z. Shan, S. C. Wu, P. He, Y. Yang, Q. H. Yang and H. S. Zhou, Consummating ion desolvation in hard carbon anodes for reversible sodium storage, *Nat. Commun.*, 2024, **15**, 3497.
49 Y. Zhou, Y. Wang, C. Fu, J. Zhou, Y. Song, S. Lin, S. Liang, S. Zhou and A. Pan, Tailoring Pseudo-Graphitic Domain by Molybdenum Modification to Boost Sodium Storage Capacity and Durability for Hard Carbon, *Small*, 2024, **20**, 2405921.
50 M. Fei, L. Qi, S. Han, Y. Li, H. Xi, Z. Lin, J. Wang, C. Ducati, M. Chhowalla, R. V. Kumar, Y. Jin and J. Zhu, Preformation of Insoluble Solid-Electrolyte Interphase for Highly Reversible Na-Ion Batteries, *Angew. Chem., Int. Ed.*, 2024, **63**, e202409719.